ORIGINAL RESEARCH ARTICLE

Ordered-Phase Equilibria in the Eutectoid Region of Bulk Fe-Pd

A. SAVOVICI, W. JENSEN, W.A. SOFFA, and J.A. FLORO

This report is the first analysis of the coexistence and microstructure of the equilibrium phases in the Fe-Pd $L1_0$ + $L1_2$ eutectoid region. Coexistence of $L1_0$ + $L1_2$ is observed at higher temperatures (650 °C), resulting in $L1_0$ polytwin plates with internal boundaries that are decorated by $L1_2$. For higher Pd content, the $L1_0$ plates are embedded in an extended $L1_2$ matrix, but the $L1_2$ wetting layers still persist. For aging at low temperatures (525 °C), L1' + $L1_2$ coexistence is observed, but the microstructure is essentially similar, except that $L1_0$ is replaced by L1'. The two-phase region is found to be much narrower than reported in published phase diagrams, of order 0.6 to 1 at pct in extent. There may be a further re-entrant narrowing below the L1' formation temperature. This work establishes L1' as a phase distinguishable from both $L1_0$ and $L1_2$, but does not yet prove that L1' is an equilibrium phase. The preferred formation of L1' at lower temperatures may relate both to stability conferred by overall ferrimagnetic interactions, and perhaps by kinetics, where L1' should have a reduced nucleation barrier from A1 relative to $L1_0$.

https://doi.org/10.1007/s11661-024-07577-4

I. INTRODUCTION

BINARY alloys of Fe-Pd binary have been studied at numerous compositions. For example, similar to Fe-Pt and Fe-Ni, compositions near 30 at pct Pd exhibit the invar effect.[1] At equiatomic compositions, the ordered $L1_0$ structure was first reported in 1938 by Hultgren *et al.*,[2] although ordering anomalies are also reported.[3] The existence of a eutectoid transformation, A1 → $L1_0$ + $L1_2$, has been established. For example, Raub *et al.*,[4] in 1963, for Fe – 62 at pct Pd samples aged at 600 °C, reported the coexistence of $L1_2$ + $L1_0$, whereas at 500 °C only single-phase $L1_0$ was found. Results such as these indicate significant knowledge gaps regarding the ordered phases, suggesting unexplained ordering phenomena or re-entrant behavior of the solvi. Despite nearly a century's worth of study in Fe-Pd, the structure and microstructure of the $L1_0$ + $L1_2$ eutectoid region have never been *directly* elucidated in the Fe-Pd binary alloy.

The published phase diagram for Fe-Pd near the eutectoid composition is reprised in Figure 1.[5] The crystal structures of interest for this report are also shown in Figure 1, where the blue (white) atoms correspond to Fe (Pd). The solid solution A1 crystal structure (Fm$\bar{3}$m, Pearson symbol cF4) decomposes into the ordered tetragonal $L1_0$ crystal structure (P4/mmm, Pearson symbol tP2) and ordered cubic $L1_2$ crystal structure (Pm$\bar{3}$m, Pearson symbol cP4) below the eutectoid isotherm ~ 760 °C. We include the L1' unit cell in Figure 1, and the approximate L1' phase field is discussed herein, and shown later in Figure 8. The L1' phase (called L' by Tetot *et al.*,[6] or ζ_1 by Shockley[7]) is another ordered tetragonal crystal structure (P4/mmm, Pearson symbol tP4) that shares the same space group as $L1_0$, but has a different Pearson symbol due to the difference in translational symmetry between the two phases.

The L1' crystal structure was first predicted as a low-temperature tetragonal phase bracketing the equiatomic composition range in Cu-Au by Shockley in 1938 using nearest-neighbor interactions (in what is now referred to as a mean-field approach).[7] His calculations were initially discounted as too simplistic, but subsequent calculations using an Ising Model[8] calculations, and the cluster variation method[6] with Monte Carlo calculations, supported Shockley's prediction. The L1' crystal structure accommodates off-stoichiometry (relative to equimolar), by distributing excess atoms solely on the (½, ½, 0) site, as opposed to distributed them equally among all complementary atoms site as happens in $L1_0$. The L1' phase was first observed indirectly in Fe-Pd thin films by Steiner *et al.*,[9] and then identified by us directly in bulk Fe-Pd.[10] The identification of L1'

A. SAVOVICI, W. JENSEN, W.A. SOFFA, and J.A. FLORO are with the Department of Materials Science and Engineering, University of Virginia, 395 McCormick Road, Charlottesville, VA 22904. Contact e-mail: as5fj@virginia.edu
Manuscript submitted May 20, 2024; accepted August 25, 2024.

Published online: 21 September 2024

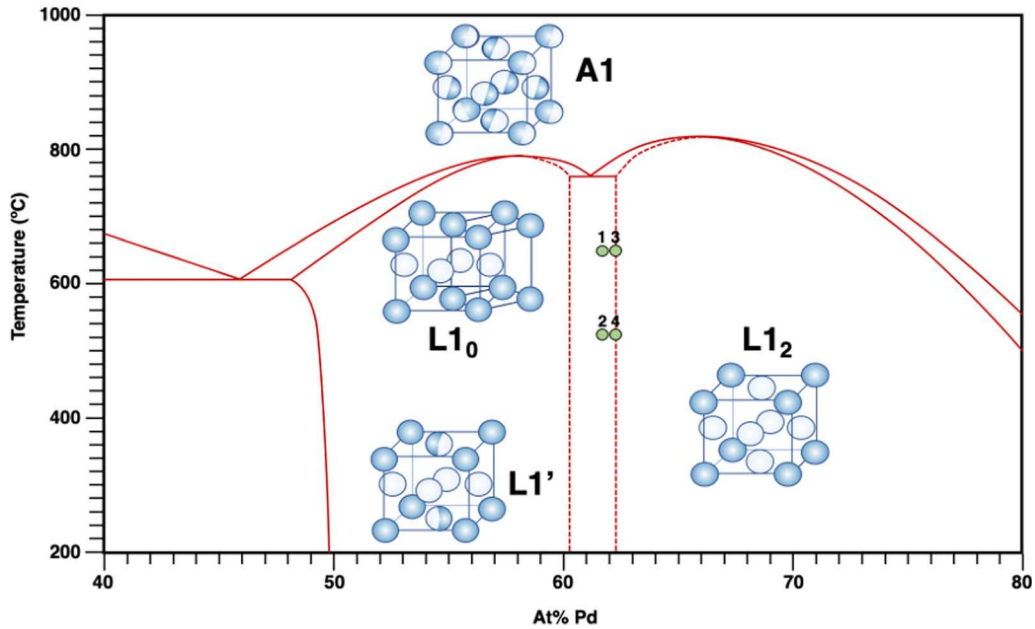

Fig. 1—A portion of the accepted Fe-Pd binary phase diagram as given by Massalski, Ref. [5]. Unit cells of the relevant phases are shown, which includes L1', whose position on the phase diagram will be shown later; blue (white) corresponds to Fe (Pd). The composition and temperatures of the four samples considered herein are shown in the nominal $L1_0 + L1_2$ region below the eutectoid isotherm (Color figure online).

is non-trivial—it has tetragonal distortion that produces peak-splitting (relative to A1) similar to $L1_0$, but has an overall structure factor that is qualitatively (but not quantitatively) similar to $L1_2$. While it may be tempting to view L1' as a metastable hybrid phase when alloy composition is intermediate to $L1_0$ and $L1_2$, this report will dispel that notion by clearly showing the coexistence of L1' + $L1_2$ at lower temperatures.

This report uses the terminology for the well known, hierarchical $L1_0$ and L1' polytwin structure given by Vlasova *et al.*[11] $L1_0$ (L1') forms with its *c*-axis oriented along any of the three principal < 100 > directions of its parent A1 matrix; as such, there are three degenerate orientation variants. To relieve the cubic → tetragonal transformation strain for A1 → $L1_0$ (or → L1'), ordered regions will twin on {110}, forming alternating regions of orthogonally oriented $L1_0$ or L1', typically referred to as "orientation variants" or "*c*-domains." In this report, local groupings of alternating *c*-domains will be referred to as a 'colony,' while the larger spatially bounded structure (that may contain one or multiple colonies) will be referred to as a 'plate.' According to Vlasova *et al.*, a collection of plates will form what is known as a 'bundle.'[11] We will use these terms for $L1_0$ & L1', as both phases adopt this hierarchical structure.

The eutectoid region of related binary alloys has been explored in the context of exchange-coupled ferromagnetism, because the magnetocrystalline anisotropy (MCA), $K_1(L1_0) \gg K_1(L1_2)$. In Co-Pt, self-assembly in these two-phase regions led to the nanochessboard structure, which exhibited tunable macroscopic magnetic properties as a function of microstructural length-scales.[12–15] Of the well-known $L1_0$ ferromagnetic systems (Fe-Pt, Fe-Pd, Co-Pt, MnAl), Fe-Pd $L1_0$ has a magnetocrystalline anisotropy, $K_1 = 1.8 \times 10^7$ ergs/cm^3, that is on the lower end of the range for these alloys, but is still much larger than most other ferromagnetic materials.[16]

II. METHODS

Two Fe-Pd boules were arc-melted from 99.99 pct Fe and 99.9 pct Pd chunks in an argon-backfilled ambient environment, with resulting nominal compositions of Fe – 61.8 at pct Pd. and Fe – 62.2 at pct Pd. The compositions were verified by inductively coupled optical emission spectroscopy (ICP-OES). In the literature, the nominal composition set by weighing the constituent elements prior to arc melting is often reported as the final composition, without further verification. However, preferential loss of one element can occur during arc melting, and so it is important to perform a post-melt assessment. This is especially true when targeting the rather narrow two-phase regions of the Fe-Pd phase diagram. Meaningful macroscale composition assessment should encompass a significant volume of material. We prefer ICP-OES to either energy-dispersive x-ray analysis (EDS) in the scanning electron microscope (SEM), or even x-ray fluorescence (XRF). However, in ICP-OES, it is still critical to assess the optimal approach to calibration.

After arc melting, subsequent thermomechanical treatments produced samples of ~ 300 μm thickness, achieved by repeated cold-rolling and recrystallization with 24-hour homogenization treatments at 1000 °C. All samples were then encapsulated in fused quartz ampules backfilled with forming gas, annealed in tube furnaces,

then water quenched. Structural analysis was performed on a Panalytical Empyrean X-ray diffractometer (XRD) with CuKa1 radiation and parallel beam θ–2 θ geometry, after polishing to 1200 grit size followed by a 3 μm diamond slurry. Microstructure was characterized using conventional transmission electron microscopy (TEM). Thin foils for TEM were prepared in a Fischione twin-jet electropolisher using an electrolyte of 82 pct acetic acid, 9 pct perchloric acid, and 9 pct ethanol (by volume) at 0 °C and approximately 30 volts. The TEM observations were performed on a ThermoFisher Titan operating at 300 kV. Magnetic measurements were conducted by a 7400 Series LakeShore vibrating sample magnetometer (VSM) on 3 mm discs punched out from the associated heat-treated samples.

Overall, four samples were investigated in detail, with two nominal compositions as given. The arc-melted samples were solutionized then water quenched to retain the high-temperature A1 phase. Subsequently, all samples were isothermally aged for either 10 or 21 days at 650 °C or 525 °C to probe phases and microstructure associated with eutectoid decomposition. These samples are given identifying numbers, 1 to 4, as shown in Figure 1.

III. RESULTS

Figure 2 shows the x-ray diffraction patterns for all four samples. Peak positions for $L1_0$, $L1_2$, and L1' were extracted from phase-pure samples. The $L1_0$ and L1' 2 θ peak assignments are the same as previously reported by us from single-phase specimens having slightly lower Pd content.[10] $L1_2$ peak assignments were made from samples that were continuously cooled through the eutectoid isotherm at various rates; this protocol produced metastable single-phase specimens. For both alloy compositions aged at 650 °C, two-phase $L1_0$ + $L1_2$ coexistence was observed, with phase fractions that depend on composition. For Pd-lean compositions (i.e., sample 2) at 525 °C, single-phase L1' was observed, as reported previously.[10] Samples 3 and 4 were Pd-rich and exhibited an $L1_2$ majority phase co-existing with $L1_0$ at 650 °C. However, aging Samples 3 and 4 at 525 °C yielded L1' + $L1_2$ coexistence (Figure 2 line 4). This is a key result, which supports the contention that L1' is a separate, stable or metastable phase at 525 °C in the range of compositions used here. For reference, the diffraction pattern of the quenched-in solid solution A1 phase is also provided in Figure S1 of Supplementary Materials.

Table I summarizes results from analysis of the XRD data for Samples 1 to 4. The lattice constants are generated from Rietveld Refinement using the GSAS-II

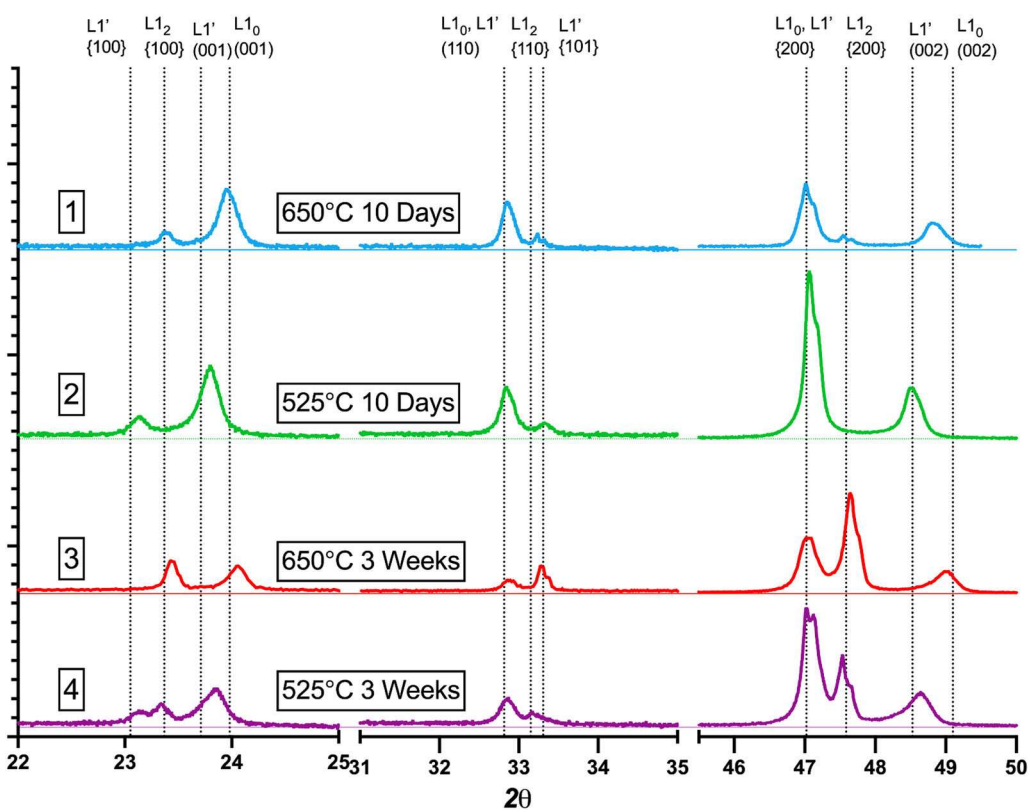

Fig. 2—X-ray diffractograms identifying the phases in bulk Fe-Pd in the eutectoid region. Sample 1: Fe – 61.8 at pct Pd aged at 650 °C displaying coexistence of $L1_0$ + $L1_2$. Sample 2: Fe – 61.8 at pct Pd aged at 525 °C yields only L1'. Samples 3 & 4: Fe – 62.2 at pct Pd); aging at 650 deg produces $L1_2$ + $L1_0$ coexistence, while aging at 525 °C produces equilibrium between L1' + $L1_2$. Notably, the volume fraction of $L1_2$ is reduced vis-à-vis $L1_0$ + $L1_2$ at high temperatures. The superlattice reflections (001) and (110) have been scaled by a factor of 3 to more clearly differentiate between the ordered phases present.

Package.[17] $L1_0$ and L1' crystals differ in their structure and ordering on the FCC sublattice sites: L1' has reduced tetragonal distortion of the unit cell (i.e, c/a is closer to unity than for $L1_0$, see Table I), and accommodates excess off-stoichiometric Pd atoms (in this case) solely on the (½, ½, 0) site, whereas $L1_0$ distributes all excess Pd equally among all Fe sites. This change in translational symmetry between $L1_0$ and L1' allows otherwise forbidden reflections in $L1_0$ to appear for L1'. These same reflections are also allowed for $L1_2$, so to fully distinguish L1' from the other ordered phases requires simultaneous coexistence of tetragonal distortion and reflections such as {100} and {101}. We show the L1'-specific reflections in Figure 2 as {100}/(001) splitting (22 to 25 deg 2 θ) and (110)/{101} splitting (31 to 35 deg 2 θ), present for both L1' (Figure 2 line 2) and L1' + $L1_2$ samples (Figure 2 line 4). Although the x-ray peak positions of each phase are sufficiently distinct, further certainty and insight are provided by also characterizing microstructure, as was done in Savovici *et al.*,[10] and is explored further below.

Of note in Table I is the dramatic change in $L1_2$ phase fraction for Pd-rich samples 3 (aged at 650 °C) and 4 (aged at 525 °C). This could indicate either a narrowing of the two-phase coexistence region in this temperature range or non-vertical solvi. Either situation would change the position on the tie line even for nominally identical system composition.

The microstructures shown in Figures 3(a) and (b) correspond to Sample 1 (Pd-lean composition), while Figures 3(b) and (c) arise from Sample 3 (Pd-rich composition), after aging at 650 °C. Sample 1 is dominated by $L1_0$ polytwin plates, which border one another, with no extended $L1_2$ phase regions visible in extended-area assessments; a representative local area is shown in Figure 3(a). However, when the internal structure of any plate, containing conjugate pairs of c-domains, is examined closely using $\boldsymbol{g}$ = (110) dark-field (DF) imaging in the TEM, illuminated lines are visible in Figure 3(b). These are nm-scale layers of the $L1_2$ phase wetting the orientation domain (ODBs) and anti-phase boundaries (APBs) of the polytwinned $L1_0$ microstructure.[18] Since Sample 1 is Pd-lean, all $L1_2$ is present *only* in these wetting layers, consistent with the small volume fraction of $L1_2$ detected by XRD in Figure 2 line 1. For Samples 3 and 4, which have Pd-rich compositions, XRD indicates a much larger volume fraction of $L1_2$ is present in equilibrium, Figures 3(c) and (d) show how this manifests in the microstructure: individual, polytwinned $L1_0$ plates are embedded within a contiguous $L1_2$ matrix (DF-TEM and associated SADP for Samples 3,4 are given in Figure4 S2 of Supplementary Materials). The $L1_0$ plates are tens of micrometers in length (or diameter, since the plates are actually disk-shaped in 3D), bounded by the original A1 grain size (see the SEM micrograph of Figure 3(c), where multiple grains are evident), but each plate has average thickness of order only 500 nm. Within each plate are alternating, conjugate pairs of c-domains, barely visible in Figure 3(d), with periodicities of order 50 nm (these are better shown in a high-resolution DF-TEM micrograph in Figure S3 of Supplementary Materials). Hence, the microstructural lengthscales are hierarchical, spanning four orders of magnitude from the nm-scale $L1_2$ wetting layers to the 50 μm plate and grain size. We also note that the microstructure of Figures 3(c) and (d), with $L1_0$ plates embedded quasi-periodically in an $L1_2$ matrix, appears to be an end-state, rather than an intermediate state, of the eutectoid decomposition.

Even in this sample with extended $L1_2$ regions, there are still $L1_2$ layers that wet the ODBs and APBs within the plates. This is shown in Figure 4, where DF imaging illuminates individual $L1_0$ variants within a plate, see Figure 4(a). In both $\boldsymbol{g}$ vector imaging conditions, the surrounding $L1_2$ matrix illuminates, since it will contribute equally to all of these superlattice reflections. Imaging with $\boldsymbol{g} = 1\bar{1}0$ in Figure 4(b) makes the plate appear dark since neither $L1_0$ orientation contributes to this reflection; however, further magnifying this plate provides direct visualization of the nanometer lengthscale $L1_2$ wetting layers that decorate the orientation domain boundaries between the two $L1_0$ variants (see inset).

The significant changes in microstructure as a function of relatively small changes in nominal Pd composition spur us to further quantify the width of two-phase coexistence region. Energy-dispersive spectroscopy (EDS) measurements performed in the TEM allow for local chemical measurements of $L1_0$ plates and the $L1_2$ matrix. Figure 3(d) shows two rectangles delineating where areal EDS scans of the $L1_0$ plate and $L1_2$ matrix. The compositions were found to have 60.8 and 61.4 at pct Pd in the $L1_0$ and $L1_2$ regions, respectively, suggesting a nominal width for the two-phase region as ~ 0.6 at pct Pd wide. Although the quantitative values disagree with the macroscopic ICP-OES results, EDS *relative* sensitivities are reported to be valid down to 0.1 at pct concentration. We had also previously created a bulk diffusion couple from two alloys whose initial compositions bound the two-phase region. Further details and the resulting SEM-EDS composition profile after annealing at 750 °C for 2 weeks are shown in Figure S4 of Supplementary Materials. The data exhibit relatively poor signal-to-noise ratio, but is still sufficient to set an upper bound of 1 at pct on the width of the $L1_0$(L1') + $L1_2$ coexistence region, consistent with the microscale TEM-EDS local measurements. This is considerably narrower than is published in existing phase diagrams.[5]

For samples aged at 525 °C, there are rather different phase fractions of the tetragonal (now L1' instead of $L1_0$) and cubic ($L1_2$) ordered phases compared with samples aged at 650 °C, even though the overall sample compositions are nominally identical. In Sample 2, only polytwinned plates of L1' are observed—$L1_2$ is NOT present, either as a matrix phase or even as wetting layers. $L1_2$ is detected by XRD in Sample 4, which is more rich in Pd, but in a much lower volume fraction relative Sample 3, having the same composition but aged at 650 °C (Sample 3). TEM shows the microstructure of Sample 4 consists of dense bundles of L1' polytwinned plates, with no $L1_2$ matrix regions, but where all L1' orientation domain and anti-phase

Table I. Lattice Constants and Weight Fractions of the Constituent Phases in the Two-Phase Samples

Sample # in Fig. 2	Phase	*a* (Å)	*c* (Å)	Wt. Frac.	*c*/*a*
1	$L1_0$	3.872	3.739	0.845	0.965
	$L1_2$	3.832	—	0.159	—
2	L1'	3.853	3.747	—	0.972
3	$L1_0$	3.877	3.735	0.21	0.963
	$L1_2$	3.831	—	0.79	—
4	L1'	3.867	3.753	0.711	0.970
	$L1_2$	3.833	—	0.282	—

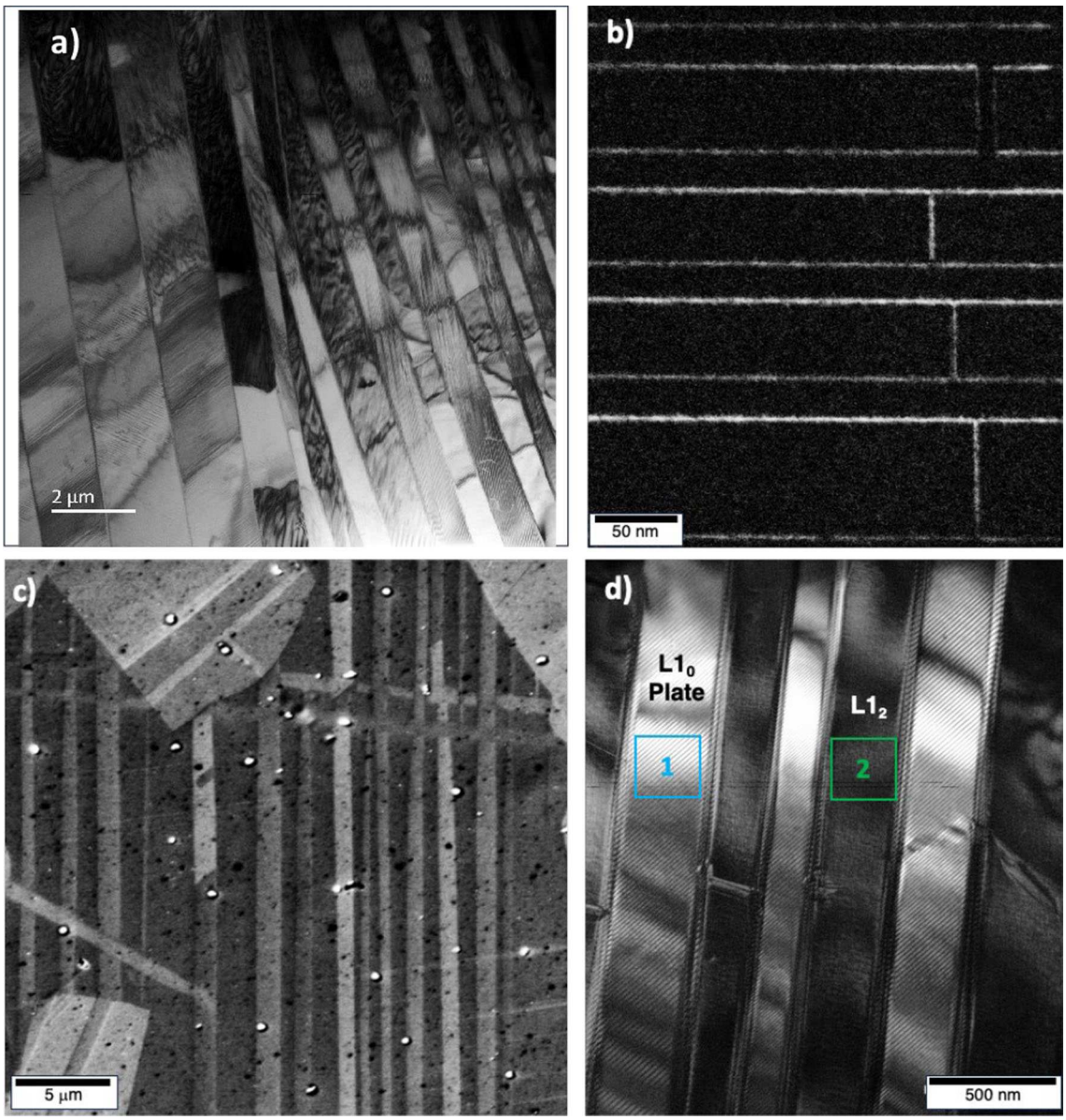

Fig. 3—Microstructure of Samples 1 (Pd-lean, panels *a*, *b*) and 3 (Pd-rich, panels *c*, *d*), after aging at 650 °C. (a) BF-TEM of a larger-scale imaging shows only polytwin $L1_0$ plates, but (b) DF-TEM with g vector (g = 110) at higher magnification reveals $L1_2$ layers wetting the orientation domain and {110}-aligned anti-phase boundaries (corresponds to Sample 1, Fig. 2 line 1). (c) The characteristic Pd-rich $L1_2$ matrix with embedded $L1_0$ plates is shown using SEM at lower magnification, while (d) shows a higher magnification BF-TEM view of the same area (sample corresponds to Fig. 2, line 3). Note that (b) was first shown in Ref. [18].

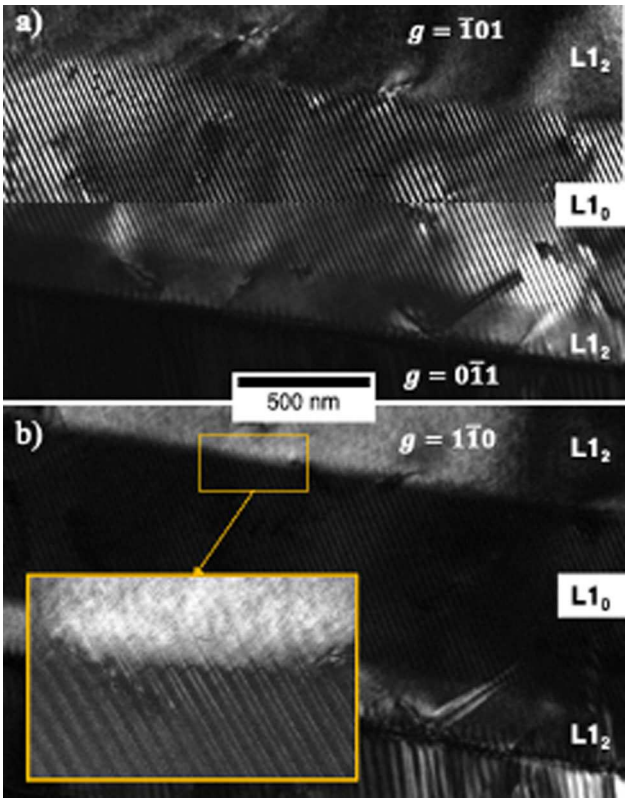

Fig. 4—DF-TEM along a [111] zone axis. (*a*) A composite image using g vectors ($g = \bar{1}01$ and $0\bar{1}1$) that illuminate each conjugate pair of *c*-domains in the $L1_0$ plate. (*b*) Shows the identical area, where $g = 1\bar{1}0$ does not light up either c-domain, but does illuminate the $L1_2$ layers wetting the ODBs. The region in the orange box is magnified inset to better show the wetting layers and the boundary with the matrix $L1_2$ (Color figure online).

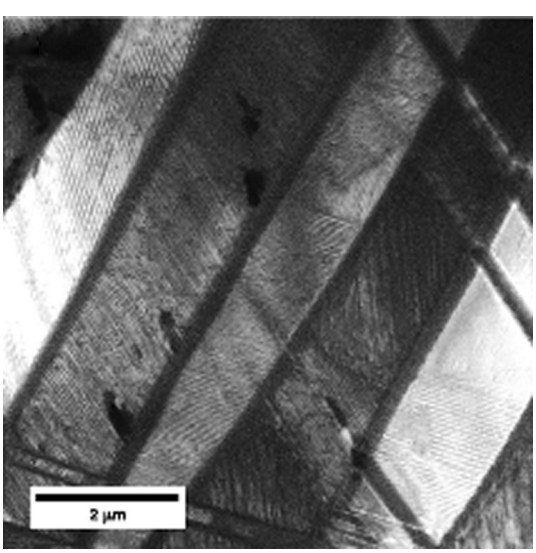

Fig. 5—BF-TEM image of Sample 4 aged at 525 deg, where XRD indicates L1' co-existing with $L1_2$ minority phase. At this magnification, only the L1' polytwin plates are imaged.

boundaries are wetted by a thin $L1_2$ region. Figure 5 shows a BF-TEM micrograph of the typical L1' polytwinned microstructure.

A series of DF-TEM micrographs from Sample 4, which is Pd-rich L1' + $L1_2$, is shown in Figure 6, using different ***g*** vectors. The change in contrast with the diffraction condition is consistent with L1' and agrees with the XRD result for this sample (Figure 2 line 4). As described previously,[10] superlattice conditions are relaxed for L1' vis-à-vis $L1_0$, so that intensity is generated from both L1' variants when viewed with imaging conditions typically used to isolate individual $L1_0$ variants. For example, in Figure 6(a) the ***g*** = (100) imaging condition produces intensity from the strong L1' *x*-variant (001) reflection and the weakly contributing L1' *y*-variant ($\bar{1}00$) reflection. Figure 6(b) shows the L1' polytwin microstructure with the ***g*** = 110 imaging condition, where both orientation domains are visible. In this figure, bright lines are the nm-scale $L1_2$ layers wetting both APBs and ODBs, as observed for the 650 °C $L1_0$ + $L1_2$ samples. These wetting layers are shown magnified in Figure 6(c), again using ***g*** = 110. As with $L1_0$ in Figure 3(b), many APBs have aligned along {110} (this image is slightly rotated for clarity), and $L1_2$ decorates all interfaces. Identically with Figure 3(b), this image shows an 'open' APB channel.[17] Figures 6(a) and (b) show a higher density of faceted APBs relative to $L1_0$ that arises in part from the increase of allowed APB translation-shift vectors (***r***) from two in $L1_0$ to three in L1'.

For completeness, magnetic hysteresis loops were gathered for all samples herein. The technical magnetic properties are unremarkable. However, changes in both the magnetic saturation and coercivity provide insight into the L1' phase vis-à-vis $L1_0$. Figure 7 compares results for single-phase $L1_0$ and L1' samples, as well as $L1_0$ + $L1_2$ produced by decomposing L1' at 700 °C; these results will be discussed below.

IV. DISCUSSION

We have established the coexistence of two ordered phases in Fe-Pd alloys at or near the A1 → $L1_0$ + $L1_2$ eutectoid. Aging at 650 °C produces $L1_0$ + $L1_2$, qualitatively consistent with published phase diagrams, while aging at 525 °C invariably produced either L1' or L1' + $L1_2$. Areally averaged EDS measurements made from the $L1_0$ and $L1_2$ phase regions show a small but resolvable composition difference, which indicates that the two-phase coexistence region is ≤ 1 at pct wide at 650 °C. As such, local composition variations of only ± 0.1 at pct will produce large relative changes in placement on the tie line, with correspondingly large changes in equilibrium phase fractions. The observed coexistence of L1' with $L1_2$ is an important result, as it confirms that L1' is a well-defined phase, and is not a metastable hybrid between $L1_0$ and $L1_2$.

We have only produced the L1' phase, whether by itself or with $L1_2$, by annealing quenched-in A1 at 525 °C. We attempted to observe the direct order-order transformation $L1_0$→L1' by aging a fully transformed $L1_0$ specimen for 41 days at 525 °C. However, no change in the $L1_0$ ordering was detected by XRD. This raises the question of whether L1' is a

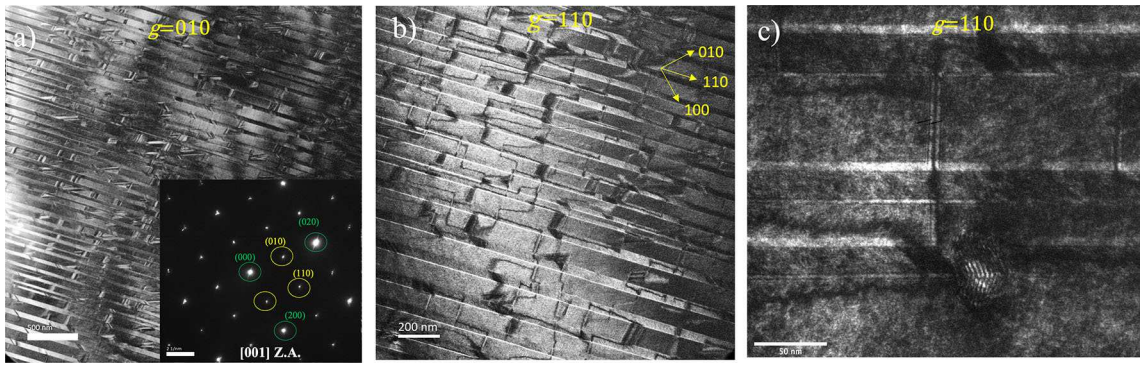

Fig. 6—DF-TEM of Sample 4 after aging at 525 °C, where XRD indicates L1' + $L1_2$ coexistence. In (*a*) and (*b*), the contrast variations with g vector are fully consistent with L1', but not with $L1_0$.[10] In (b), thin wetting layers of $L1_2$ along all of the L1' ODB and APBs are seen as bright lines. (*c*) Higher magnification using the same ***g*** vector as in panel (b), showing more clearly the thicker ODB wetting layers of $L1_2$, as well as the wet and faceted APBs.

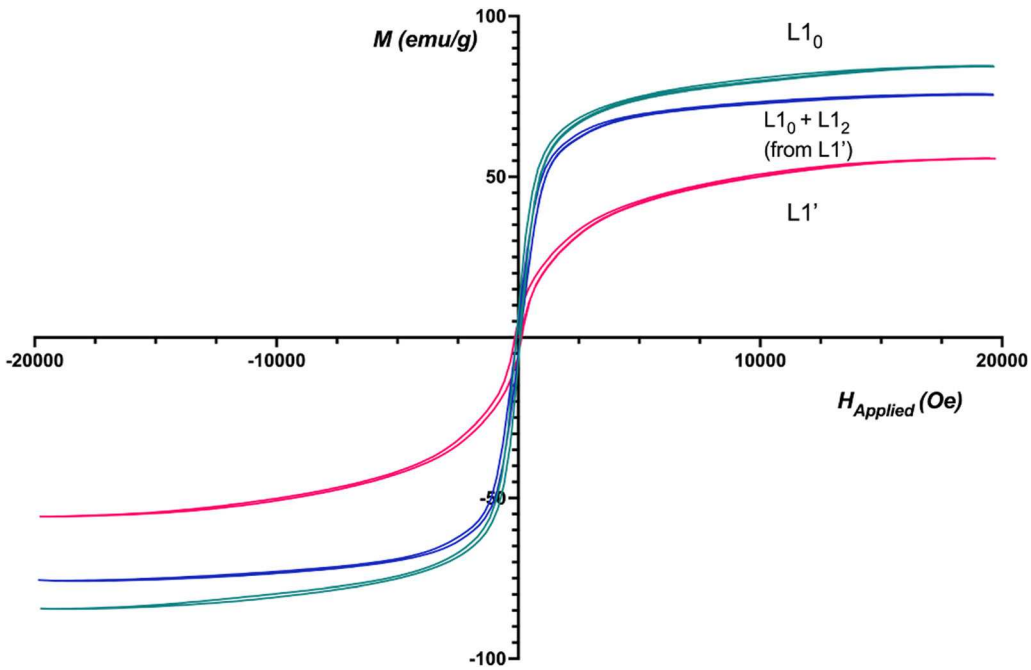

Fig. 7—Hysteresis loops for single-phase $L1_0$ (green), L1' (red), and 2-phase $L1_0$ + $L1_2$ produced by annealing the L1' at 700 °C. Specific properties are summarized in Table II (Color figure online).

metastable phase—its preferred formation from A1 at lower temperatures would be consistent with a reduced nucleation barrier for L1', anticipated since its c/a ratio is closer to unity than is c/a for $L1_0$, thus reducing the increase in elastic energy upon ordering. However, direct formation of L1' from $L1_0$ as an equilibrium transformation could simply be kinetically suppressed, where the driving force is expected to be quite small and since diffusion is known to be more difficult in ordered phases than in their disordered counterparts.[19–21]

Conversely, we have annealed fully formed L1' for 45 days at 525 °C and found no tendency to revert to $L1_0$. This lends some credence to the contention that L1' is in fact a stable phase, but again sluggish kinetics could frustrate equilibration to $L1_0$. L1' *does* readily decompose to $L1_0$ + $L1_2$ at higher temperatures, as shown in the XRD results of Figure 8(a), for annealing at 700 °C for 40 days. This formation of $L1_0$ + $L1_2$ from L1' upon higher temperature annealing suggests a retrograde narrowing of the two-phase region at lower temperatures. This is also supported by the difference found in $L1_2$ phase fractions (see Table I), for the Pd-rich Samples 3 and 4 aged at 650 °C vs. 525 °C. Additionally, results by Raub *et al.*,[4] can be explained by this narrowing of the two-phase region. Figure 8(b) shows a portion of the Fe-Pd phase diagram, amended based on the results obtained. One primary modification is the much narrower two-phase region, which results directly from our TEM-EDS measurements of adjacent $L1_0$ and (coarse) $L1_2$ relative phase compositions (microstructure shown in Figures 3(c) and (d)). The eutectoid is also shifted to larger Pd contents relative to

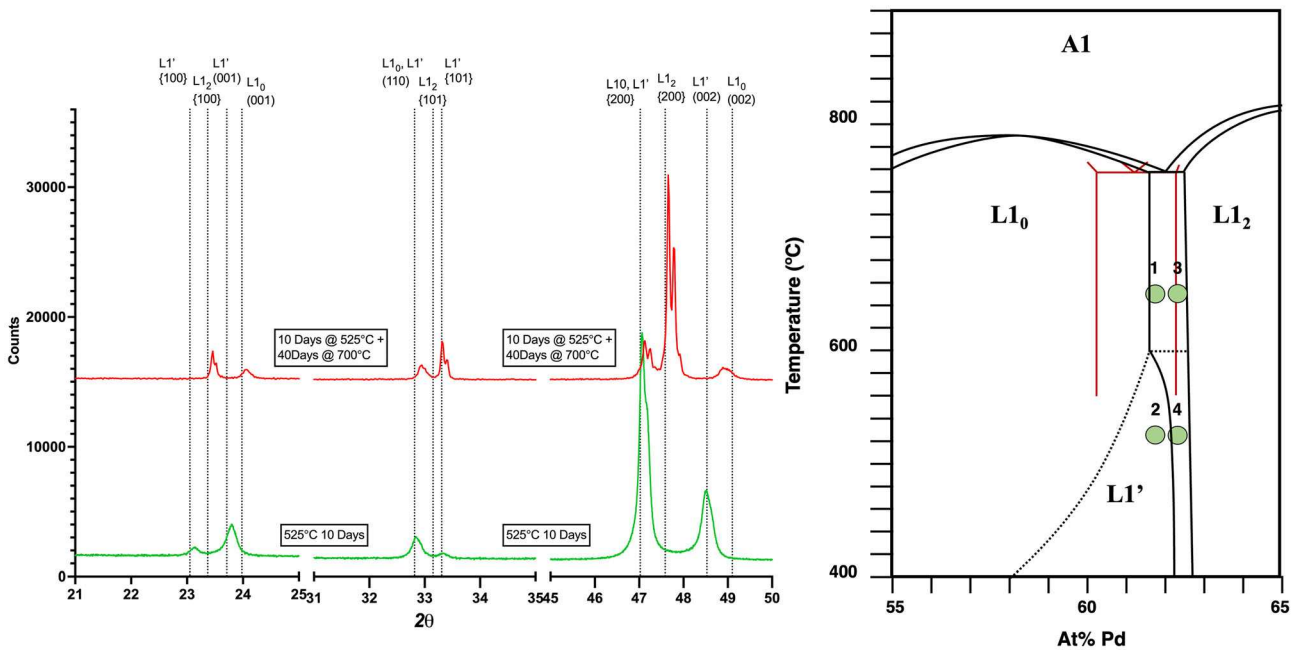

Fig. 8—The diffractograms in (*a*) show a single-phase L1' sample (green) transforms to $L1_0$ + $L1_2$ after aging for 1000 hrs at 700 °C (red). An amendment to the eutectoid phase diagram is shown in (*b*), with the originally published 2-phase region depicted in red (Color figure online).

the published diagram—this comes from the ICP-OES measurements of the overall alloy compositions of samples 1 and 2. Figure 8(b) includes the addition of an L1' phase field, coupled with a retrograde narrowing of the two-phase region starting with the intersection with the L1' phase boundary. The boundary position is only approximate, as we have not determined the exact composition-temperature dependence. We also show this $L1_0$/L1' boundary as a 2nd or higher-order transition (a "locus of critical points" [22]). A higher-order transition $L1_0 \rightarrow$ L1' is allowed by group symmetry considerations, but the transformation order is not experimentally confirmed. In Figure 8(b), we have not modified either the eutectoid isotherm temperature nor the maximum disorder/order temperatures of the $L1_0$ and $L1_2$ phases, since these were not interrogated herein.

Microstructure in the two-phase coexistence region for $L1_0$ + $L1_2$ is characterized by the presence of $L1_0$ in the form of polytwinned plates, with $L1_2$ exhibiting two different morphologies—wetting layers formed on orientation domain boundaries that separate alternating *c*-variants of the $L1_0$ polytwins, and, for higher Pd content, also an extended matrix phase of $L1_2$ (c.f., Figures 3 and 4). The stable embedding of $L1_0$ plates in an $L1_2$ matrix, while it could be anticipated from tie-line considerations, appears to be a new observation in the literature.

Related microstructures are obtained in Pd-rich samples aged at 525 °C, but where L1' now co-exists with $L1_2$ that again forms as a wetting layer, analogous to what was found in $L1_0$ + $L1_2$. However, the $L1_2$ wetting layers for L1' + $L1_2$ were observed to be thicker, with extended regions easily surpassing 5 nm, consistent with a larger phase fraction for sample 4 in Table I. With decreased tetragonality in L1' vis-à-vis $L1_0$, coherency strain is reduced, allowing thicker wetting layers to be energetically stable.

The coexistence of L1' + $L1_2$ supports the view that L1' is a unique phase, rather than being a kinetically trapped hybrid configuration for alloy compositions intermediate to $L1_0$ and L1'. The order (in the Ehrenfest classification[23]) of the transformation between $L1_0$/L1' has been contested in the past, with Shockley[7] calculating a latent heat, consistent with a first-order (nucleation + growth) transformation. Utilizing CVM calculations, Tetot *et al.*,[6] predicted that the transformation L10 $\rightarrow$ L1' was second order, while $L1_2 \rightarrow$ L1' transformation would be first order. L1' has also been predicted as a metastable phase in the low-temperature Ni-rich Ni-Al system, as shown by Calphad calculations, and was predicted to have a second-order transformation with $L1_0$.[24]] Our current results do not discern the transformation order.

Magnetic properties can provide insight into the ordered phases and their microstructure. As shown in Figure 8 and Table II, L1' consistently exhibits 35 pct lower magnetic saturation moment, M_s, than $L1_0$, which suggests that magnetic coupling of Fe and Pd may differ in the two phases. Conversion of M_s, in emu/g to Bohr magnetons is calculated using $\mu_{(f.u.)} = \frac{(M_s)(m_r)}{(\mu_B)(N_A)} * 10^{-3}$, (in Bohr magneton per formula unit), where M_s is in emu/g), m_r is the molar mass in gram/mol, μ_B is the Bohr magneton (J/T), and N_A is Avogadro's number. Total moments per unit cell for $L1_0$ and L1' are shown in Table II. We next examine whether the observed differences between moment/unit cell can be reproduced by assuming ferromagnetic coupling between all species for $L1_0$ and ferrimagnetic coupling between Fe & Pd for L1'.

Table II. Observed Magnetic Saturation, Coercivity, and Calculated Magnetic Bohr Magnetons Per Unit Cell for $L1_0$ and L1'

Crystal Structure	M_S(emu/cm^3)	Coercivity (Oe)	Mol. Weight (g/mol)	Total Moment/Unit Cell (μ_B)
$L1_0$	886.3	81.5	349.2	5.39
L1'	578	138.1	349.2	3.52

Lyubina *et al.*, obtained temperature-dependent atomic moments using neutron diffraction of nanocrystalline $Fe_{40}Pd_{60}$ alloys, close to our composition of 62 at pct Pd, that produced by cryomilling, finding μ_{Fe} = 2.75 μ_B and μ_{Pd} = 0.3 μ_B.[25] We take the 4 atoms per pseudocubic unit cell for both $L1_0$ and L1' to be distributed as 1.5 Fe atoms and 2.5 Pd atoms, giving a composition of 62 at pct Pd. Using the species-dependent moments from Lyubina *et al.*, a total moment/unit cell for $L1_0$ of 4.88 μ_B is predicted, about 10 pct lower than our magnetometry value of 5.39 μ_B. For L1', making an *ad hoc* assumption of antiferromagnetic coupling between Fe and Pd for L1', we obtain a total moment/unit cell of 3.38 μ_B, about 4 pct lower than our measured value of 3.52 μ_B. If we accept these values as a reasonable level of agreement (more on this below), then we assert that the inherent site disorder on (001) planes associated with L1' ordering produces an effective ferrimagnetic behavior, where all Pd moments are opposite to the Fe moments.

It is interesting and non-trivial that the moments obtained by Lyubina *et al.*, using neutron diffraction, *underestimate* the total moment we observe in both the $L1_0$ and L1' phases, but especially in the former. Our magnetometer is calibrated against a Ni standard before each measurement, so magnetization values are considered sound. We estimate, using the moments of Lyubina *et al.*, that our composition would have to be 57 at pct Pd, rather than 62 at pct Pd, in order to reproduce the total moment/unit cell. This large an error in the composition, determined by calibrated ICP-OES, seems untenable. Alternatively, the values for the Fe and Pd moments obtained by Lyubina *et al.*, may be too low. Notably, they report an $L1_0$-order parameter of S = 0.78 for their alloy, whereas our samples have S = 0.92. Atomic moments may depend on the order parameter. Using first principles calculations, both Burzo and Vlaic,[26] and Pathak *et al.*,[27] found for stoichiometric Fe-Pd at 0K that ordering does not affect the Fe moment much, but does increase the Pd moment by 15-21 pct, at 0K. However, a comparison of experimental values obtained by Lyubina *et al.*, for stoichiometric $L1_0$ (S = 0.7) against values measured by Cable *et al.*, for stoichiometric A1,[28] both at room temperature, implies that moments are *lower* on both Fe and Pd in the ordered $L1_0$ phase. Hence, it is not clear if differences in order parameter can explain the underestimation of the total moment. At this time, we cannot provide a self-consistent explanation for the underestimation of the measured $L1_0$ moment using the species-dependent values from Lyubina *et al.*[25]

To complete the comparison, we note that the lattice parameters in Table I agree with those reported for $Fe_{40}Pd_{60}$ by Lyubina *et al.*, to within 1 pct.[25] Given the likely differences in strain in the mechanically alloyed nanocrystalline samples vs. bulk polytwin, this is thought to be reasonable agreement.

The coercivity of our $L1_0$ phase is about 3× lower than stoichiometric Fe-Pd $L1_0$ formed in bulk by thermomechanical treatments, reported by Zhang and Soffa.[29] They suggest that pinning of domain walls controls magnetization reversal, and analyzed the macroscopic coercivity as $H_c \propto \frac{DFK_1^{3/2}}{A^{1/2}M_s}$, where D is the effective dimension of the pinning site (they suggested APB's were the pinning defect), F is the area fraction of the domain wall interacting with pinning sites at any instant, A is the exchange coupling constant, and K_1 is the anisotropy constant, here dominated by the first component of the magnetocrystalline anisotropy. M_s is again the saturation magnetization. We next take the ratio of the observed coercivities in our alloys (composition 62 at pct Pd) to the stoichiometric (50 at pct Pd) alloy of ZS. To simplify, we assume the same pinning sites are active, so the D's are identical, and take A(62) to 0.83A(50), crudely based on the variation of the Curie temperature vs. composition in Fe-Pd $L1_0$ alloys,[30] giving:

$$\frac{H_c(62)}{H_c(50)} = 1.2\left(\frac{F(62)}{F(50)}\right)\left(\frac{K_1(62)}{K_1(50)}\right)^{3/2}\left(\frac{M_s(50)}{M_s(62)}\right) \quad [1]$$

From Zhang & Soffa, $H_c(50)$ = 250 Oe, and M_s = 1100 emu/cm^3.[28] Substituting these, and the corresponding values for 62 at pct Pd $L1_0$ alloys from Table II, into Eq. [1] and solving for the ratio of pinning site area fractions, gives

$$\frac{F(62)}{F(50)} = 0.37\left(\frac{K_1(50)}{K_1(62)}\right)^{3/2} \quad [2]$$

From Reference 31 we take $K_1(50)/K_1(62)$ = 2.5, so we find that the pinning site density of our alloy would need to be 1.5x larger than the stoichiometric alloy. Given the estimates employed here, this essentially implies that the two compositions should have roughly similar pinning site area fractions in order to explain the observed magnetic properties, and that does appear to be the case, at least with regard to APB density.

We can perform a similar analysis for the coercivity values in Table II comparing $L1_0$ and L1' at

compositions near 62 at pct Pd. We obtain the same result as Eq. [2], except where the numerical prefactor has a value of 1.1. We do not know quantitatively how K_1(L1') compares to $K_1(L1_0)$, but it should be smaller given the reduced tetragonality and the nature of the ordering. We note that $L1_2$ alloys are calculated to have a magnetocrystalline anisotropy energy that is 10x smaller than $L1_0$ (both are taken to be stoichiometric[27]), setting an lower bound for L1'. Assuming that K_1 is 5-10x smaller for L1', we conclude that the pinning site density must arrive be 12-35x larger in L1' than $L1_0$. L1' will have at least a 3/2x x increase in APB density relative to $L1_0$, intrinsically arising from the higher translational symmetry of L1' vis-à-vis $L1_0$, where more translational shift vectors are allowed. There may also be an extrinsic contribution to the APB density associated with the lower temperature processing required to form L1' from A1. So the estimates are again reasonable, but the assumption that APB's are the actual pinning sites remains to be proven.

V. CONCLUSIONS

The $L1_0$–$L1_2$ coexistence region in the Fe-Pd phase diagram is considerably narrower in extent than reported previously, spanning less than 1 at pct at 650 °C. In consequence, alloy processing for applications will be very challenging, as even small deviations from the desired composition, whether macroscopic (sample average), or microscopically (local fluctuations), will greatly affect the amounts of the tetragonal and cubic ordered phases.

The coexistence of $L1_0$ and $L1_2$ is accommodated in two ways. $L1_0$ itself occurs as highly anisotropic, disk-shaped plates; within each plate a conjugate pair of *c*-axis variants alternates in the classic polytwin microstructure. For relatively small fractions of $L1_2$, the cubic phase forms as nm-scale layers coherently wetting both the planar boundaries between the polytwin variants, and a subset of the anti-phase boundaries. The thickness of the wetting layers adjusts based on the equilibrium volume fraction along the tie line, but there is likely a maximum thickness determined by elastic energy considerations. For larger $L1_2$ fractions (more Pd), $L1_2$ forms an extended matrix phase, with the $L1_0$ polytwin plates embedded in a parallel, quasi-periodic arrangement. The $L1_2$ wetting layers present within the $L1_0$ plates are retained even when the extended $L1_2$ matrix phase is present. This observation, along with highly anisotropic $L1_0$ plate morphologies, and their quasi-periodic arrangement in the $L1_2$ matrix, poses interesting questions with regard to the mechanisms for the ordering transformation that will be considered in a later publication.

The L1' phase, first predicted in 1938, appears consistently at lower temperatures near 62 at pct Pd, and can exist both as a single phase or in coexistence with $L1_2$, depending on Pd content of the parent alloy. The presence of this phase appears to produce a retrograde narrowing of the solvus, L1'/L1' + $L1_2$. While we have not definitively proven that L1' is an equilibrium phase, or whether there is a first- or higher-order transformation from $L1_0 \leftrightarrow$ L1', magnetic ordering may directly impart L1' stability at low temperatures. CVM calculations indicated only a very slight stability conveyed by chemical bonding considerations.[6] We hypothesize that additional stability is conveyed by magnetic interactions, although this will require first principles modeling to confirm. Of course, even if L1' is a stable phase at 525 °C, it must disappear as temperatures approach absolute zero, since only stoichiometric phases are possible at 0 K in accord with the Third Law of thermodynamics.

ACKNOWLEDGMENTS

Our thanks to Prof. Bi-Cheng Zhou for useful discussions. Extensive use of the UVA Nanoscale Materials Characterization Facility is greatly appreciated. This work was supported by the National Science Foundation under Grant DMR-1709914.

CONFLICT OF INTEREST

On behalf of all authors, the corresponding author states that there is no conflict of interest.

SUPPLEMENTARY INFORMATION

The online version contains supplementary material available at https://doi.org/10.1007/s11661-024-07577-4.

REFERENCES

1. H. Shima, K. Oikawa, A. Fujita, K. Fukamichi, and K. Ishida: *Proc. Int. Conf. Magn. ICM 2003*, 2004, vol. 272–276, p. 2173.
2. R. Hultgren and C.A. Zapffe: *Z. Für Krist. - Cryst. Mater.*, 1938, vol. 99, p. 509.
3. N.M. Kleinerman, V.V. Serikov, N.I. Vlasova, and A.G. Popov: *Philos. Mag.*, 2018, vol. 98, p. 2380.
4. E. Raub, H. Beeskow, and O. Loebich: Das Zustandsbild Eisen-Palladium Unterhalb 950°C vol. 54, p. 549 (1963).
5. Massalski, T.B., Okamoto, H., Subramanian, P.R., and Kacprzak, L., *Binary Alloy Phase Diagrams, 2nd Ed.*, 2nd ed. (ASM International, Materials Park, OH, 1990).
6. R. Tétot, A. Finel, and F. Ducastelle: *J. Stat. Phys.*, 1990, vol. 61, p. 121.
7. W. Shockley: *J. Chem. Phys.*, 1938, vol. 6, p. 130.
8. A. Finel and F. Ducastelle: *Europhys. Lett.*, 1986, vol. 1, p. 135.
9. M.A. Steiner, R.B. Comes, J.A. Floro, W.A. Soffa, and J.M. Fitz-Gerald: *Acta Mater.*, 2015, vol. 85, p. 261.
10. A. Savovici, W.A. Soffa, and J.A. Floro: *Scr. Mater.*, 2023, vol. 234, 115540.
11. N.I. Vlasova, G.S. Kandaurova, and N.N. Shchegoleva: *J. Magn. Magn. Mater.*, 2000, vol. 222, p. 138.
12. E.P. Vetter, L. Geng, P. Ghatwai, D.A. Gilbert, Y. Jin, W.A. Soffa, and J.A. Floro: *APL Mater.*, 2016, vol. 4, 096103.
13. J.A. Floro, E.P. Vetter, P. Ghatwai, L.D. Geng, Y.M. Jin, and W.A. Soffa: *J. Magn. Magn. Mater.*, 2019, vol. 487, 165313.
14. L.D. Geng, W.A. Soffa, J.A. Floro, and Y.M. Jin: *J. Appl. Phys.*, 2018, vol. 123, 093901.
15. I. Kashyap, E.P. Vetter, J.A. Floro, and M. De Graef: *J. Magn. Magn. Mater.*, 2019, vol. 479, p. 204.
16. T. Klemmer, D. Hoydick, H. Okumura, B. Zhang, and W.A. Soffa: *Proc. Acta Metall Meet. Nov. Magn. Struct. Prop.*, 1995, vol. 33, p. 1793.
17. B.H. Toby and R.B. Von Dreele: *J. Appl. Crystallogr.*, 2013, vol. 46, p. 544.
18. A. Savovici, Y.M. Jin, W.A. Soffa, and J.A. Floro: *Scr. Mater.*, 2024, vol. 246, 116067.
19. A.B. Kuper, D. Lazarus, J.R. Manning, and C.T. Tomizuka: *Phys. Rev.*, 1956, vol. 104, p. 1536.
20. Y. Iijima and C.-G. Lee: *Acta Metall. Mater.*, 1995, vol. 43, p. 1183.
21. A. Kushida, K. Tanaka, and H. Numakura: *Mater. Trans. Jim*, 2003, vol. 44, p. 59.
22. W.A. Soffa and D.E. Laughlin: 8 - Diffusional Phase Transformations, in *The Solid State, in Physical Metallurgy*, 5th ed., D.E. Laughlin and K. Hono, eds., Elsevier, Oxford, 2014, pp. 851–1020.
23. G. Jaeger: *Arch. Hist. Exact Sci.*, 1998, vol. 53, p. 51.
24. S. Tumminello, M. Palumbo, J. Koßmann, T. Hammerschmidt, P.R. Alonso, S. Sommadossi, and S.G. Fries: *Metals*, 2020, vol. 10, p. 1.
25. J. Lyubina, O. Gutfleisch, and O. Isnard: *J. Appl. Phys.*, 2009, vol. 105, p. 07A717.
26. E. Burzo and P. Vlaic: *J. Optoelectron. Adv. Mater.*, 2010, vol. 12, p. 1869.
27. R. Pathak, O.A. Golovnia, E.G. Gerasimov, A.G. Popov, N.I. Vlasova, R. Skomski, and A. Kashyap: *J. Magn. Magn. Mater.*, 2020, vol. 499, 166266.
28. J.W. Cable, E.O. Wollan, and W.C. Koehler: *Phys. Rev.*, 1965, vol. 138, p. A755.
29. B. Zhang and W.A. Soffa: *Phys. Status Solidi A*, 1992, vol. 131, p. 707.
30. L. Wang, Z. Fan, A.G. Roy, and D.E. Laughlin: *J. Appl. Phys.*, 2004, vol. 95, p. 7483.
31. N. Miyata, H. Asami, T. Mizushima, and K. Sato: *J. Phys. Soc. Jpn.*, 1990, vol. 59, p. 1817.